Materials Advances

ROYAL SOCIETY OF CHEMISTRY

PAPER

View Article Online
View Journal

Check for updates

Cite this: DOI: 10.1039/d6ma00033a

Highly stable fluorescent coordination polymer materials for the ultrafast detection of nitrofurans in aqueous media at ppb levels

Alokananda Chanda and Sanjay K. Mandal *

Received 7th January 2026,
Accepted 21st March 2026

DOI: 10.1039/d6ma00033a

rsc.li/materials-advances

The unsupervised usage and uncontrolled disposal of antibiotics into water bodies have detrimental effects on human health, aquatic life, and agriculture. Thus, several research studies have been conducted to detect the presence of trace amounts of such antibiotics *via* cost-effective and user-friendly fluorescence-based techniques. In this work, we report the synthesis of four luminescent coordination polymers (CPs), $\{[Co(oxdz)(bpma)(H_2O)]\cdot H_2O\}_n$ (**1**), $\{[Ni(oxdz)(bpma)(H_2O)]\}_n$ (**2**), $\{[Zn(oxdz)(bpma)]\cdot 2H_2O\}_n$ (**3**), and $\{[Cd(oxdz)(bpma)]\cdot 4H_2O\}_n$ (**4**), with d^7 (Co(II)), d^8 (Ni(II)), and d^{10} (Zn(II) and Cd(II)) metal centers, respectively, utilizing an ancillary ligand, N,N′-bis(pyridylmethyl)methylamine (bpma), and a bent dicarboxylate, 4,4′-(1,3,4-oxadiazole-2,5-diyl)-dibenzoate ($oxdz^{2-}$). Based on their single-crystal X-ray structures, these CPs exhibit different helicities depending on the geometry and coordination number preference of the metal center, the capping nature of bpma (facial *vs.* meridional) and the binding of the dicarboxylate groups of $oxdz^{2-}$ (monodentate *vs.* bidentate). All the CPs have high thermal stability. To demonstrate their use, these CPs have been employed for the selective and ultrafast detection of trace levels of nitrofuran-based antibiotics in aqueous media. Among these, CP **4** exhibits the best efficiency (K_{SV} values of 6.77×10^4 M^{-1} and 5.86×10^4 M^{-1}, respectively) and high sensitivity (LOD values of 197 and 172 ppb, respectively) toward nitrofurantoin (NFT) and nitrofurazone (NFZ). Its ultrafast response during real-life application (65% quenching in 20 s) and recyclability up to five times without any loss in efficiency make CP **4** eligible to safeguard human health and aquatic lives from the perilous effects of nitrofuran-based antibiotics.

Introduction

In the last few decades, a sharp rise in the consumption of antibiotics has been observed due to a number of reasons, such as human population growth, increased life expectancy, and advancement in modern medical facilities.[1–3] These antibiotics, although revolutionary in the field of medicine, are found to be nonbiodegradable and persist in the environment for a long period of time. The uncontrolled disposal of nonbiodegradable antibiotics into water systems can disrupt the ecosystem balance.[4] Large amounts of antibiotics discarded by pharmaceutical industries and sewage treatment plants have been detected in water bodies, contributing to the development of multidrug-resistant bacteria and posing a threat to aquatic life. Furthermore, living organisms are known to catabolise these antibiotics partially; thus, only 30% of these antibiotics are absorbed, while the remaining are excreted as ingested residues in soil and water bodies.[5] For instance, nitrofurantoin, a nitrofuran-based antibiotic that is widely used to cure bacterial infection in the urinary tract, can cause liver disorder, immunity decline, and even cancer when consumed by a normal individual without any supervision.[6] Nitrofurazone, another nitrofuran-based antibiotic, has therapeutic values, but it is found to be mutagenic and carcinogenic.[7,8] In order to eliminate this issue, doctors from several countries have either stopped prescribing or have limited the usage of certain antibiotics. Despite that, a significant amount of several antibiotics is still found in lakes, rivers, underground water, subsidiary agricultural products, and milk. Thus, considering all the above-mentioned facts, different classes of antibiotics have emerged as serious organic pollutants, and consequently, their detection has become a hot topic globally.

Earlier, in order to mitigate this serious issue, several sophisticated techniques, such as high-performance liquid chromatography (HPLC) mass spectrometry, liquid chromatography (LC) mass spectrometry, electrochemical methods, and capillary electrophoresis (CE), have been explored.[6,9–12] However, these techniques have several drawbacks, including the involvement of expensive and single-analyte-directed devices, complicated pretreatment processes, and the requirement of

Department of Chemical Sciences, Indian Institute of Science Education and Research Mohali, Sector 81, Manauli PO, S.A.S. Nagar, Mohali, Punjab 140306, India. E-mail: sanjaymandal@iisermohali.ac.in

Open Access Article. Published on 24 April 2026. Downloaded on 5/16/2026 2:45:13 AM.
This article is licensed under a Creative Commons Attribution-NonCommercial 3.0 Unported Licence.

Open Access Article. Published on 24 April 2026. Downloaded on 5/16/2026 2:45:13 AM.
This article is licensed under a Creative Commons Attribution-NonCommercial 3.0 Unported Licence.

extensive period of time. For instance, some of the disadvantages of the HPLC technique are that it requires a large amount of solvents, exhibits peak tailing, and demands high economic investments. Both HPLC and LC are sophisticated techniques but are not portable. Likewise, sensitivity is a great concern when utilizing the CE technique for the detection of a trace amount of an analyte. This issue arises as it requires the injection of a low volume of the sample in the capillary as well as the association of a short optical path length.

For some time, photoluminescence-based sensors have provided a solution to all the above-mentioned challenges. In this context, luminescent metal–organic coordination networks (LMOCNs) that include both 1D coordination polymers (CPs) and 2D/3D metal–organic frameworks (MOFs) are strategically designed with π-conjugated motifs and appropriate interaction sites, which play a crucial role in the sensitive and selective detection of nitro-explosives, ketones and aldehydes, toxic metal ions, volatile organic molecules, antibiotics, and other hazardous small molecules.[13–20] In these LMOCNs, the π-conjugated motifs act as the signalling unit, and the interaction sites act as the recognition unit.[21] These crystalline materials with the proper alignment of signalling-recognition units can efficiently detect a very trace amount of the analyte for up to a significant number of cycles and, most importantly, in seconds. In the literature, most of the LMOCNs reported for the detection of antibiotics are based on lanthanides and d^{10}-metal centers, where primarily turn-off responses are observed.[20,22–50] Moreover, the detection of nitrofuran-based antibiotics in aqueous media with very low LOD values is very rarely reported in the literature.

Considering the salient features of LMOCNs and the urgency of the detection of antibiotics, we hypothesize that the combination of a bent dicarboxylate with a five-membered oxadiazole moiety, $oxdz^{2-}$, and a tridentate capping N-donor ligand, bpma, as shown in Scheme 1, can generate a series of desired LMOCNs. The oxadiazole moiety is capable of enhancing the fluorescence quantum yield and exhibits fluorescence emission near the blue region.[19,20,51–53] Additionally, the two N atoms in the five-membered ring of oxadiazole can act as H-bond-accepting sites, which provides scope for facile interactions with antibiotics.[20] The meridional and facial bindings of the tridentate capping ligand to the metal center highly depend on the coordination number preference of the metal center. Thus, both the capping of bpma to the metal center and the alignment of $oxdz^{2-}$ generate different helical arrangements of the coordination polymers to allow enough scope of close proximity of sensors with the analytes through supramolecular interactions. Based on our recent success in detecting such analytes with very low LODs using an LMOCN containing a d^{10} metal center, $oxdz^{2-}$ and a noncapping N-donor ligand,[20] we further utilized the bpma capping ligand and the d^7 and d^8 metal centers for a detailed comparative study.

Herein, we report the synthesis of four CPs, $\{[Co(oxdz)(bpma)(H_2O)]\cdot H_2O\}_n$ (**1**), $\{[Ni(oxdz)(bpma)(H_2O)]\}_n$ (**2**), $\{[Zn(oxdz)(bpma)]\cdot 2H_2O\}_n$ (**3**), and $\{[Cd(oxdz)(bpma)]\ 4H_2O\}_n$ (**4**), with varied helicities *via* a one-pot self-assembly pathway under ambient conditions utilizing the respective metal acetates, bpma, and $oxdz^{2-}$. These materials were explored for the detection of nitrofuran-based antibiotics in aqueous media. Amongst all the CPs, **4** exhibited the maximum quenching and could effectively detect two nitrofuran-based antibiotics, NFT and NFZ, in aqueous media within 20 s, providing limit of detection values as low as 197 ppb (0.831 μmol L^{-1}) for NFT and 172 ppb (0.869 μmol L^{-1}) for NFZ. The stability of **4** in the presence of NFT and NFZ solutions was confirmed by the unchanged PXRD patterns and FTIR spectra. Additionally, it could maintain its efficiency for up to five cycles. The mechanism of action was further elaborated through a combination of spectral overlap analysis and theoretical calculations to understand the results of this study.

Experimental section

All chemicals and solvents obtained from commercial sources were utilized for synthesis without further purification under aerobic conditions. Some part of this section is available in the SI. The ancillary ligands bpma and H_2(oxdz) were prepared according to the reported procedures.[54,55] $\{[Cd(mbhna)(bpma)]\cdot DMF\}_n$ (**5**) and $\{[Cd(3,7\text{-DBTDC})(bpma)]\ H_2O\}_n$ (**6**), where

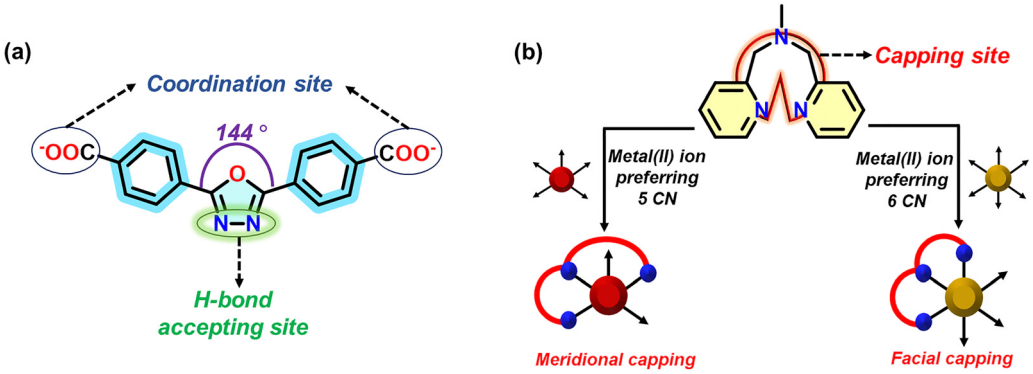

Scheme 1 Structures of (a) $oxdz^{2-}$, marked with the coordination sites and hydrogen bond-accepting sites, and (b) bpma, showing its facial and meridional binding options to a metal center.

© 2026 The Author(s). Published by the Royal Society of Chemistry

Open Access Article. Published on 24 April 2026. Downloaded on 5/16/2026 2:45:13 AM. This article is licensed under a Creative Commons Attribution-NonCommercial 3.0 Unported Licence.

mbhna^{2-} = (4,4′-methylene-bis(3-hydroxy-2-naphthalene carboxylate)) and 3,7-DBTDC^{2-} = benzothio-phene-5,5′-dioxide-3,7-dicarboxylate, were made according to the reported methods.[17,56] Their identities and purities were verified by matching the spectroscopic (FTIR) data and powder X-ray diffractograms with the reported ones (Fig. S1).

Synthesis of {[Co(oxdz)(bpma)(H$_2$O)]H$_2$O}$_n$ (1)

In a 10 mL round-bottom flask, 25 mg (0.1 mmol) of Co(OAc)$_2$·4H$_2$O was dissolved in 1 mL of methanol. To this, a methanolic solution containing 21 mg (0.1 mmol) of bpma was added and stirred for 15 min. An aqueous solution of Na$_2$(oxdz) (31 mg, 0.1 mmol and 1 mL of water) was then added to this clear solution, and the formation of a pink precipitate was observed immediately. The mixture was stirred for 12 h at room temperature. The pink solid was filtered, washed several times with water and methanol, and air-dried. Yield: 47 mg (76%). Anal. calcd for $C_{29}H_{27}CoN_5O_7$ (MW = 616.50): %C, 55.50; %H, 4.41; %N, 11.36; found: %C, 55.9; %H, 4.1; %N, 11.4. Selected FTIR peaks (KBr, cm^{-1}): 3432 (br), 1607 (s), 1587 (s), 1387 (s), 1020 (s), 812 (s) and 730 (w).

Synthesis of {[Ni(oxdz)(bpma)(H$_2$O)]}$_n$ (2)

In a 10 mL round-bottom flask, 25 mg (0.1 mmol) of Ni(OAc)$_2$·4H$_2$O was dissolved in 1 mL of methanol. To this, a methanolic solution containing 21 mg (0.1 mmol) of bpma was added and stirred for 15 min. An aqueous solution of Na$_2$(oxdz) (31 mg, 0.1 mmol and 1 mL of water) was then added to this clear solution, and the formation of a light-green precipitate was observed immediately. The mixture was stirred for 12 h at room temperature. The green solid was filtered, washed several times with water and methanol, and air-dried. Yield: 51 mg (85%). Anal. calcd for $C_{29}H_{25}N_5NiO_6$ (MW = 598.24): %C, 58.22; %H, 4.21; %N, 11.71; found: %C, 58.4; %H, 4.2; %N, 11.2. Selected FTIR peaks (KBr, cm^{-1}): 3457 (br), 1607 (s), 1570 (s), 1384 (s), 1025 (s), 820 (s) and 729 (w).

Synthesis of {[Zn(oxdz)(bpma)]·2H$_2$O}$_n$ (3)

In a 10 mL round-bottom flask, 22 mg (0.1 mmol) of Zn(OAc)$_2$·2H$_2$O was dissolved in 1 mL of ethanol. To this, an ethanolic solution containing 21 mg (0.1 mmol) of bpma was added and stirred for 15 min. An aqueous solution of Na$_2$(oxdz) (31 mg, 0.1 mmol and 1 mL of water) was then added to this clear solution, and the formation of a white precipitate was observed immediately. The mixture was stirred for 12 h at room temperature. The white solid was filtered, washed several times with water and methanol, and air-dried. Yield: 57 mg (92%). Anal. calcd for $C_{29}H_{27}N_5O_7Zn$ (MW = 622.94): %C, 55.91; %H, 4.37; %N, 11.24; found: %C, 55.7; %H, 4.27; %N, 11.66. Selected FTIR peaks (KBr, cm^{-1}): 3415 (br), 1628 (s), 1579 (s), 1387 (s), 1020 (s), 767 (s) and 726 (w).

Synthesis of {[Cd(oxdz)(bpma)]·4H$_2$O}$_n$ (4)

In a 10 mL round-bottom flask, 27 mg (0.1 mmol) of Cd(OAc)$_2$·2H$_2$O was dissolved in 1 mL of ethanol. To this, an ethanolic solution containing 21 mg (0.1 mmol) of bpma was added and stirred for 15 min. An aqueous solution of Na$_2$(oxdz) (31 mg, 0.1 mmol and 1 mL of water) was then added to this clear solution, and the formation of a white precipitate was observed immediately. The mixture was stirred for 12 h at room temperature. The white solid was filtered, washed several times with water and methanol, and air-dried. Yield: 52 mg (77%). Anal. calcd for $C_{29}H_{31}CdN_5O_9$ (MW = 706.01): %C, 49.34; %H, 4.43; %N, 9.92; found: %C, 50.11; %H, 4.2; %N, 9.57. Selected FTIR peaks (KBr, cm^{-1}): 3428 (br), 1604 (s), 1571 (s), 1449 (w), 1392 (s), 1020 (s), 867 (s) and 726 (w).

Suitable crystals of **2–4** were obtained by layering the ethanolic/methanolic solution of respective metal salts and the bpma ligand over a buffer of ethanol–water/methanol–water that was layered over the aqueous solution of Na$_2$(oxdz). Our attempts to get suitable crystals of **1** were unsuccessful.

Fluorescence measurements

In a typical experiment for the solvent study, 1 mg of the sample (finely ground) was added to 2 mL of a particular solvent taken in a quartz cuvette (10 mm path length) and constantly stirred to form a uniformly dispersed suspension to record its emission spectrum. Similarly, for the fluorescence titration experiments of various antibiotic-based analytes like nitrofurantoin (NFT), nitrofurazone (NFZ), furazolidone (FDZ), ornidazole (ODZ), dimetridazole (DMZ), sulfamethazine (SMZ), and sulfadiazine (SDZ), 1 mg of the sample dispersed in 2 mL of Milli-Q water was taken in a quartz cuvette, followed by the incremental addition of analytes from a 1 mM stock solution (prepared in 9 mL of Milli-Q water and 1 mL of methanol) to record the corresponding emission spectra. The addition of 1 mL of methanol was required to dissolve certain antibiotic solids, which were otherwise difficult to dissolve in pure Milli-Q water.

For the test paper strip experiment, test strips were prepared by soaking TLC plates in an aqueous dispersion of **4** for 15 min, followed by drying in air. On these test strips, NFT or NFZ antibiotics (30 μL) were drop-casted for their real-time detection under a UV light, displaying a blue color.

The lifetime measurements of pristine **4**, as well as those in the presence of different concentrations of NFT or NFZ, were executed using a picosecond time-correlated single-photon counting system (model: Horiba Jobin Yvon) equipped with a pulse diode laser with a constant repetition rate of 1 MHz and a time-to-amplitude converter in the range of 200 ns (0.055 ns per channel). The concentration of NFT/NFZ was varied from 0 to 150 μL with a repetition rate of 1 MHz (kept constant). Each lifetime decay profile was generated and analyzed with the DAS 6.3 software for a triexponential fitting for **4** with an acceptable value of $\chi^2 = 1 \pm 0.2$.

Results and discussion

Synthesis and structural analysis

A one-pot self-assembly method using equivalent amounts of the metal salt, oxdz^{2-}, and bpma in a methanol–water or ethanol–water mixture at 25 °C was utilized to obtain **1–4** in

Open Access Article. Published on 24 April 2026. Downloaded on 5/16/2026 2:45:13 AM.
This article is licensed under a Creative Commons Attribution-NonCommercial 3.0 Unported Licence.

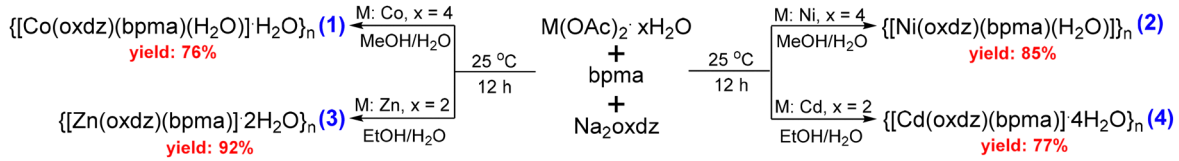

Scheme 2 Syntheses of **1–4** under ambient conditions.

good yields (Scheme 2). This process can easily be scaled up with the same isolated yield without the application of any external source of energy. These CPs were elaborately characterized by elemental analysis, FTIR spectroscopy, X-ray diffraction (single-crystal and powder), thermogravimetric analysis, scanning electron microscopy (SEM) and transmission electron microscopy (TEM). In the solid-state FTIR spectra of **1–4** (Fig. S2–S5), broad bands appear in the range of 3415–3457 cm^{-1} due to the O–H stretching of coordinated and/or lattice water molecules. On the other hand, the difference between the asymmetric and symmetric stretching frequencies is used to predict the binding modes of a carboxylate group with metal ions.[57] For instance, a difference greater than 220 cm^{-1} (220 cm^{-1} in **1**, 223 cm^{-1} in **2**, and 241 cm^{-1} in **3**) suggests that the dicarboxylate groups of $oxdz^{2-}$ bind to the metal center in the monodentate mode. Interestingly, two sets of asymmetric and symmetric stretching frequencies are observed in **4**, indicating the existence of both the bidentate chelating and monodentate binding modes of $oxdz^{2-}$, respectively. On the other hand, the presence of the same carboxylate binding mode in **1** and **2** indicates their structural similarity.

Single-crystal X-ray diffraction reveals that **2** crystallizes in the orthorhombic space group *Pnma* (Table S1). Its asymmetric unit comprises a Ni(II) ion, one $oxdz^{2-}$ linker, one bpma ligand, and one coordinated water molecule (Fig. S6a). Each metal center in the 1D polymeric chain is found to be hexa-coordinated, forming a distorted octahedral geometry. As shown in Fig. 1a, Ni(II) is coordinated with three nitrogen atoms from one bpma ligand, three oxygen atoms from two different $oxdz^{2-}$ linkers, and one coordinated water molecule, thereby exhibiting an N_3O_3 geometry. The coordinated water is strongly intermolecularly hydrogen bonded to the uncoordinated oxygen atoms of the $oxdz^{2-}$ linkers. The bpma ligand caps the metal ion in the facial mode (the values of N_{alkyl}–Ni–N_{py} and N_{py}–Ni–N_{py} angles are 82.55° and 85.83°, respectively), as shown in the expanded inset of Fig. 1a. The Ni–N_{py} distance is found to be 2.0674 Å, whereas the Ni–N_{alkyl} distance is 2.122 Å. The facial capping by bpma leaves open coordination sites on the metal center for the dicarboxylate to bind. The $oxdz^{2-}$ binds to the metal centers in the monodentate mode with its two ends, resulting in a broad U-shaped 1D coordination polymer with a separation of 17.74 Å between the Ni(II) centers. The Ni–O_{carb} distance is found to be 2.0617 Å, which matches well with that of other $oxdz^{2-}$-based frameworks reported in the literature.[58,59]

Similar to **2**, compound **3** is also a 1D coordination polymer that crystallizes in the monoclinic space group $P2_1/c$ (Fig. 1b and Table S1). As shown in Fig. S6b, the asymmetric unit consists of one Zn(II) center, one bpma, one $oxdz^{2-}$, and disordered lattice water molecules (squeezed out in the final refinement). The metal center is found to be penta-coordinated with an N_3O_2 environment, forming a distorted trigonal bipyramidal geometry, which is confirmed by the τ parameter being

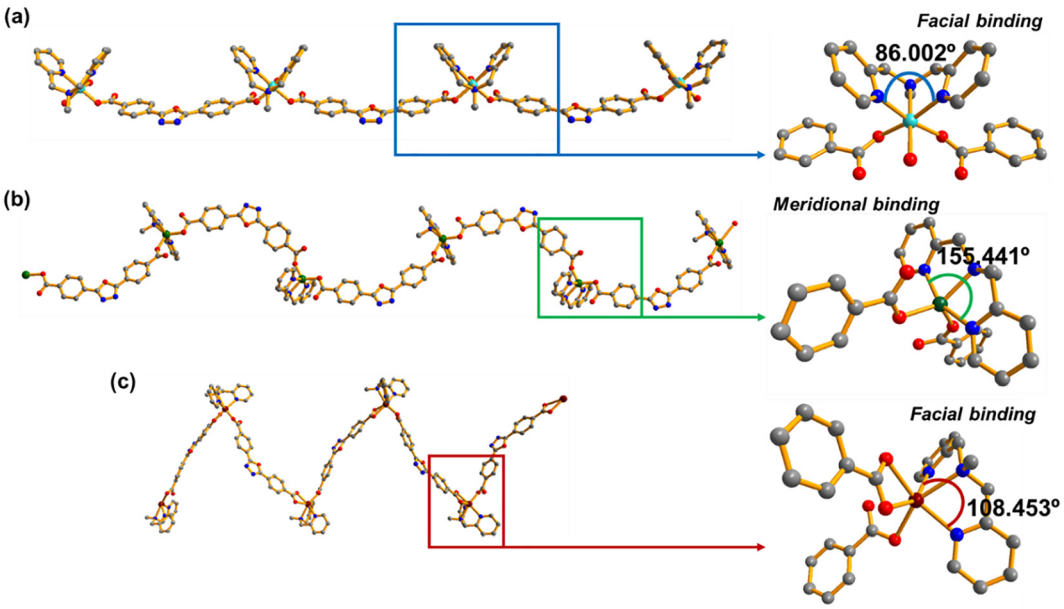

Fig. 1 (a)–(c) Structural features of **2–4** along with the binding modes of bpma (facial and meridional) and $oxdz^{2-}$, respectively.

© 2026 The Author(s). Published by the Royal Society of Chemistry

Open Access Article. Published on 24 April 2026. Downloaded on 5/16/2026 2:45:13 AM.
This article is licensed under a Creative Commons Attribution-NonCommercial 3.0 Unported Licence.

close to 1.[60] Unlike **2**, the bpma ligand in **3** binds to the metal center in the meridional mode with an N_{py}–Zn–N_{py} angle of 155.441° and N_{alkyl}–Zn–N_{py} angles ranging from 77.3° to 78.2° (the expanded inset of Fig. 1b). The Zn–N_{py} distances range from 2.104 to 2.132 Å, whereas the Zn–N_{alkyl} distance is found to be 2.165 Å. The dicarboxylate binds to the metal ion in the monodentate mode with its two ends. This results in a U-shaped helical 1D coordination polymer with a separation of 16.08 Å between the Zn(II) centers. The Zn–O_{carb} distances range from 1.978 to 2.010 Å. These values are similar to those reported in the literature.[19,61]

Compound **4** is also a 1D coordination polymer that crystallizes in the orthorhombic space group *Pbcn* (Fig. 1c and Table S1). As shown in Fig. S6c, the asymmetric unit consists of one Cd(II) center, one bpma, one $oxdz^{2-}$, and disordered lattice water molecules (squeezed out in the final refinement). In the polymer, each of the metal centers is found to be hexa-coordinated with an N_3O_3 environment, forming a distorted octahedral geometry (Fig. 1c).

Similar to **2**, the bpma ligand in **4** binds to the metal center in the facial mode with an N_{py}–Cd–N_{py} angle of 108.8° (the expanded inset of Fig. 1c), while the N_{alkyl}–Cd–N_{py} angles range from 70.2° to 71.2°. The Cd–N_{py} distances range from 2.344 to 2.35 Å, whereas the Cd–N_{alkyl} distance is found to be 2.454 Å. The dicarboxylate binds to the metal ion in the monodentate mode with one end and in the bidentate chelating mode with the other end. This arrangement of the capping ligand and dicarboxylate with the metal center leads to a V-like helical 1D coordination polymer with a separation of 18.14 Å between the Cd(II) centers. The Cd–O_{carb} distances range from 2.269 to 2.425 Å, which is similar to those reported in the literature.[62]

According to the structures of **2–4**, the bpma ligand wraps the five-coordinated and six-coordinated metal centers in meridional and facial modes, respectively. Thus, the difference in the helicity of the 1D coordination polymers occurs due to the difference in the binding modes of the capping ligand (facial and meridional), the preferred coordination number of the metal ions, and the angularity and alignment of the bent dicarboxylate.

The packing diagrams of **3** and **4** (Fig. 2) were assessed for the existence of supramolecular interactions between the adjacent helical chains. In **3** and **4**, a moderate π···π interaction (3.75 Å and 3.56 Å, respectively) exists between two adjacent chains, leading to the parallel staggered stacking of the oxadiazole moiety (from one $oxdz^{2-}$ linker) and the benzene ring (from another $oxdz^{2-}$ linker).

The bulk phase purity of **2–4** was confirmed by powder XRD analysis. As shown in Fig. 3, the experimental powder patterns of **2–4** corroborate well with their respective simulated patterns (obtained from single-crystal data), confirming their phase purity. The PXRD pattern of **1** indicates that it is highly crystalline and it is isostructural to **2**. A comparison of the PXRD patterns of the as-synthesized **3** and its crystals, which were used for its single-crystal structure determination (*vide supra*), shows some line broadening and minor shifts of a few peaks (Fig. 3b). This prompted us to remeasure the diffractogram several times using three different instruments. However, we found that the inherent nature of the packing of the particles may be responsible for this observation. To further confirm this, the FTIR spectra of the as-synthesized **3** and its crystals were compared to show an exact match (Fig. S7).

In order to establish the chemical stability, compound **4** (as an example and its detailed study for the sensing experiments, *vide infra*) was soaked in water, methanol, and solutions with different pH (pH 5, 7, and 9) for three days, after which its PXRD pattern was recorded and compared with that of the as-synthesized compound (Fig. S8 and S9). The PXRD patterns of the treated compounds match well with those of the as-synthesized **4**, confirming the retention of its structural features.

The TG analysis of **1–4** was carried out between 30 °C and 500 °C under a dinitrogen atmosphere to determine their

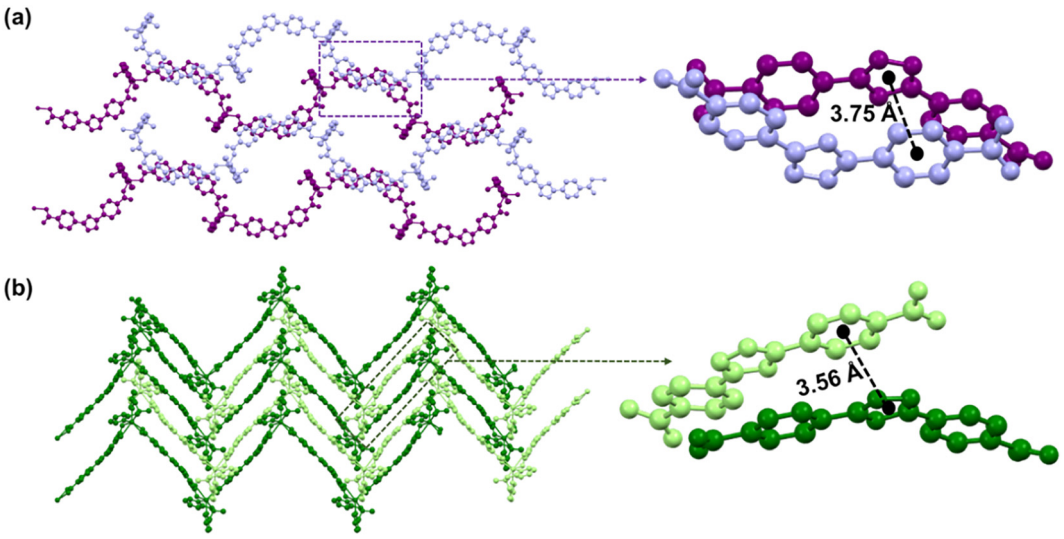

Fig. 2 (a) and (b) Packing diagrams of **3** and **4**, respectively, indicating the existence of moderate π···π interactions between adjacent layers, leading to the formation of the respective supramolecular assemblies.

Open Access Article. Published on 24 April 2026. Downloaded on 5/16/2026 2:45:13 AM.
This article is licensed under a Creative Commons Attribution-NonCommercial 3.0 Unported Licence.

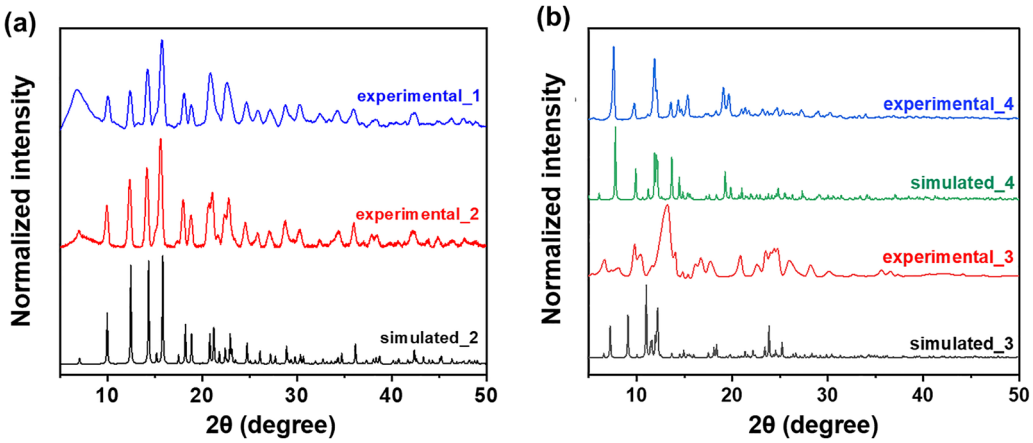

Fig. 3 (a) and (b) Simulated and PXRD patterns of **1–4**, respectively.

thermal stability (Fig. S10). While **1**, **2**, and **4** are stable beyond 230 °C, **3** is stable up to 316 °C. Compound **1** exhibits a weight loss of 6.2% (calculated: 6.2%) due to the removal of one coordinated water molecule and one lattice water molecule. Compound **2** exhibits a weight loss of 2.91% (calculated: 3%) due to the removal of one coordinated water molecule. For **3**, a one-step weight loss (6%) is observed, corroborating the removal of two lattice water molecules (calculated: 5.7%). For **4**, a one-step weight loss (10.2%) is observed between 30 °C and 89 °C due to the removal of four lattice water molecules (calculated: 10.2%).

The morphological study of the as-isolated **1–4** was performed using FESEM analysis (Fig. 4a–d). The FESEM images of **1–4** indicate that these are aggregations of very tiny, irregular particles. Their morphology was further evaluated using TEM images (Fig. 4e–h). The distribution of the respective elements on the surface of **1–4** was confirmed by EDX elemental mapping, as shown in Fig. 4i–l and Fig. S11. The HRTEM image of **4** shows very prominent lattice fringes, from which the *d*-spacing value was calculated using the inverse fast Fourier transform (IFFT), and it is found to be 0.257–0.293 nm, corresponding to the *hkl* values (5 0 3) and (6 1 2), respectively (Fig. 4m). Additionally, the definite SAED pattern of **4** provides additional confirmation of its crystallinity, as shown in Fig. 4n. The average particle size of **4**, as determined from the particle size distribution plot, as shown in Fig. 4o, is found to be 1.9 micron.

Photophysical properties. In order to understand the effect of metal ions on the absorption profiles, the solid-state diffuse reflectance spectra of **1–4** were analysed (Fig. S12). The peaks observed in the region of 210–267 nm are due to the π–π* transition, while the peaks in the region of 295–308 nm are observed due to the n–π* transition within the ligand system.[20] The peaks at 488 nm (**1**) and 594 nm (**2**) are due to the d–d transitions contributed by the Co(II) and Ni(II) ions, respectively. Such a transition is not observed for **3** and **4**, as expected from the d^{10} metal ion in the coordination networks.

Utilizing the Tauc plot shown in Fig. S13, the band gap energy values for **1–4** were calculated. The intercept on the *x*-axis obtained by extrapolating the linear portion of the curve gave the band gap energy values. The calculated band gap values for **1**, **2** and **4** are similar (around 3.5 eV), whereas **3** exhibits the lowest value (3.25 eV). These results corroborate well with those for a reported MOCN constructed with $oxdz^{2-}$.[59]

Detection of nitrofurans. Because contaminated water from different water reservoirs entering the human body can have severe effects, it is important to carry out luminescent sensing of organic pollutants in aqueous media. Therefore, before commencing with any fluorescence experiment using the uniform suspensions of **1–4** in water, the stability of **4** (as an example) in water was assessed using PXRD. The same PXRD patterns (as shown in Fig. S8) are recorded before and after soaking in water for three days, confirming the retention of its structural integrity.

The emission spectra of the uniform suspensions of **1–4** in water were recorded by exciting at 310 nm (Fig. S14). Upon the incremental addition of 150 μL of a 1 mM solution of NFT (in a mixture of Milli-Q water and methanol, 9 : 1 v/v) to the uniform suspensions of **1–4**, a gradual drop in their emission intensity is observed (Fig. 5 and Fig. S15, S16). The maximum quenching is exhibited by **4** (91%), followed by **3** (80%), **1** (76%) and **2** (75%). This observation corroborates well with the fact that CPs of d^{10} metal ions are preferred over the CPs of transition metal ions with partially filled d-orbitals as luminescent chemosensors. While the presence of the oxadiazole moiety and the π-conjugated aromatic rings in the CPs results in linker-based emission, d^{10} metal ions amplify their luminescent properties as it leaves no scope for energy decay due to d–d transitions.

After observing the maximum quenching exhibited by **4** toward NFT, we extended our efforts to determine the effect of other antibiotics, such as FDZ, DMZ, SMZ, and SDZ, on its emission (Fig. 6a). Compared with NFT (91%), other analytes quench the emission intensity of **4** to a lesser extent: FDZ (60%), SDZ (20%), DMZ (15%), and SMZ (13%). Therefore, the selectivity of **4** is evident toward NFT. In order to generalize this trend, the response of **4** toward another nitrofuran-based antibiotic, nitrofurazone (NFZ), was also checked with the quenching trend (shown in Fig. 6b) as follows: NFZ (89%) > ODZ (58%) > DMZ (15%) > SMZ (13%) > SDZ (20%). This confirms that **4** is also selective toward NFZ.

© 2026 The Author(s). Published by the Royal Society of Chemistry

Open Access Article. Published on 24 April 2026. Downloaded on 5/16/2026 2:45:13 AM.
This article is licensed under a Creative Commons Attribution-NonCommercial 3.0 Unported Licence.

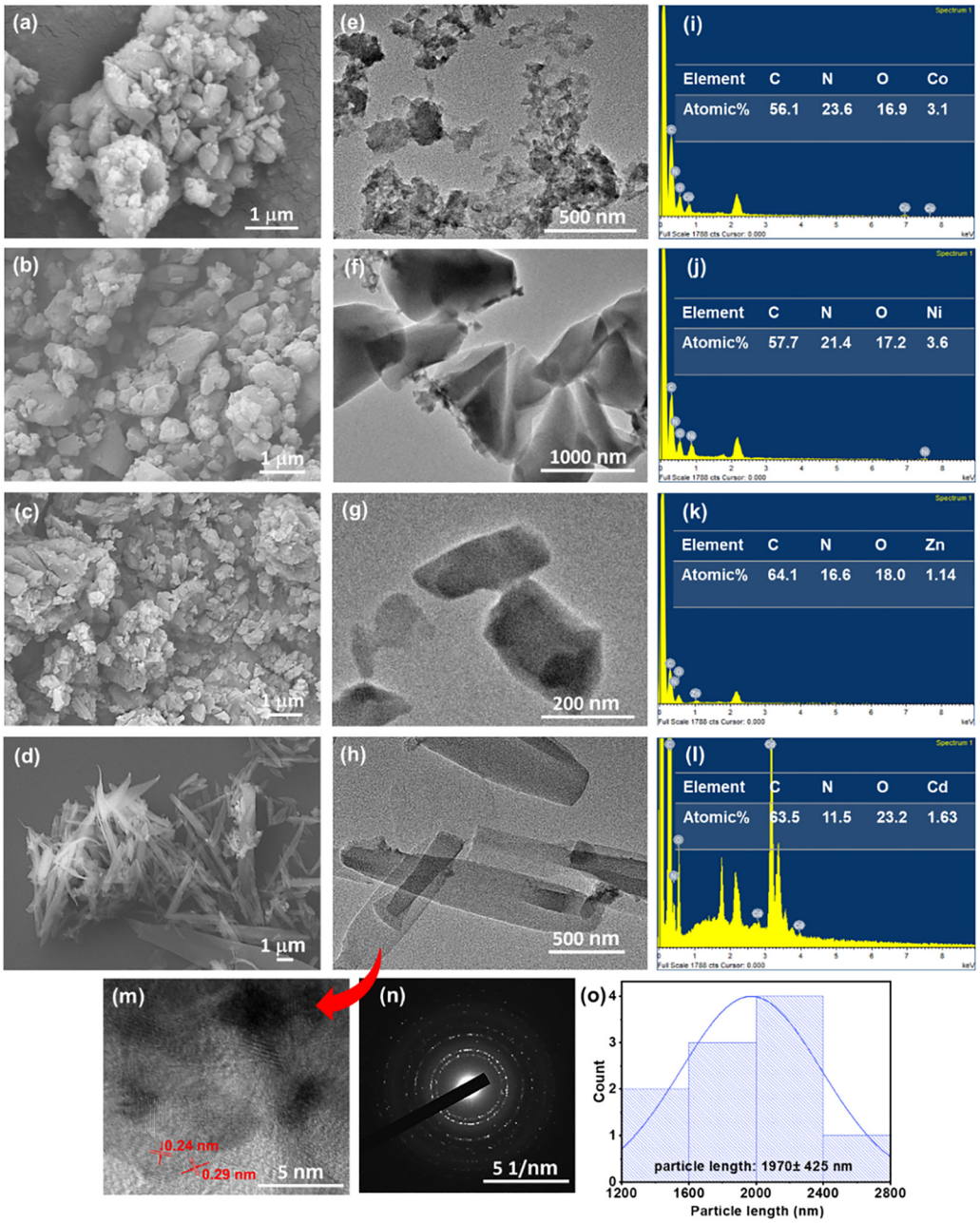

Fig. 4 (a)–(d) FESEM images of **1–4**, respectively. (e)–(h) TEM images of **1–4**, respectively. (i)–(l) EDX analysis of **1–4**, respectively. (m) HRTEM image of **4** showing its distinct lattice fringes. (n) SAED pattern of **4**. (o) Particle size distribution plot for **4**.

This quenching trend by the antibiotics can be explained with the help of three probable factors: (i) supramolecular interactions (hydrogen bond and π···π interactions) between the sensor and the antibiotics, (ii) an electron transfer from the electron-rich sensor to the electron-deficient antibiotics, and (iii) an energy transfer from the sensor to the analyte. For the nitro group-bearing antibiotics, NFT and NFZ, it is assumed that all three considerations come into play, and thus, they exhibit the maximum quenching. For other nitro group-bearing antibiotics like FDZ, ODZ, and DMZ and non-nitro antibiotics like SMZ and SDZ, a moderate-to-low quenching is observed. Though these antibiotics provide scope for supramolecular interactions with the sensor, the extent of energy overlap is less, and also, for SMZ or SDZ, the electron transfer is not possible at all. These observations highlight the roles of both electron transfer (PET) and energy overlap (FRET) in the quenching process (*vide infra*).

The Stern–Volmer equation, $I_0/I = 1 + K_{SV}[Q]$ (where I_0 and I are the emission intensities of the framework before and after the addition of an analyte, respectively; K_{SV} is the quenching constant and [Q] is the concentration of the quencher), is widely used to determine the extent of interaction between the sensor and the analyte at low concentrations. It follows the principle that the greater the interaction, the higher the K_{SV} value, leading to a significant amount of quenching.

Open Access Article. Published on 24 April 2026. Downloaded on 5/16/2026 2:45:13 AM.
This article is licensed under a Creative Commons Attribution-NonCommercial 3.0 Unported Licence.

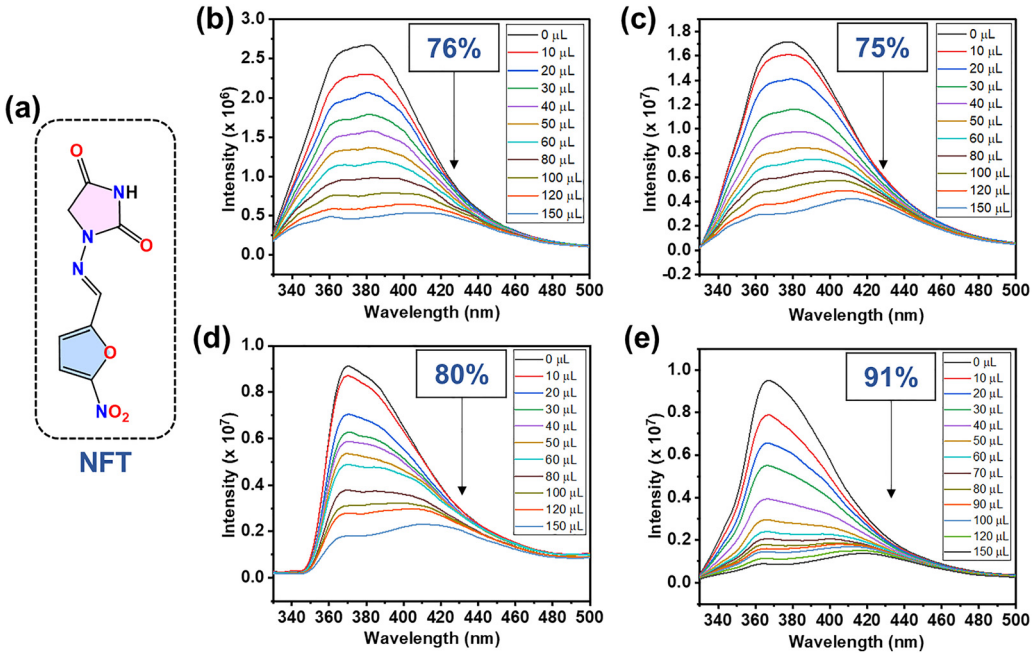

Fig. 5 (a) Structure of nitrofurantoin (NFT). (b)–(e) Fluorescence titration plots for **1–4**, respectively, by NFT (1 mM) (λ_{exc} = 310 nm).

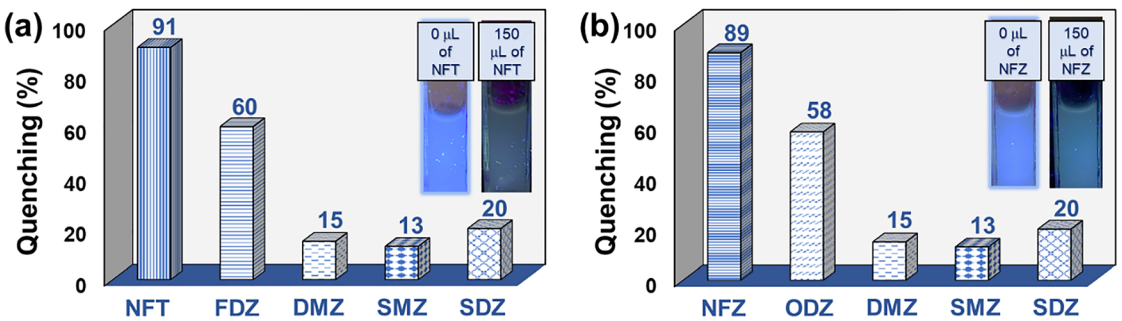

Fig. 6 (a) and (b) Selectivity of **4** toward NFT and NFZ, respectively.

Interestingly, the V-shaped helicity exhibited by **4** provides a greater number of accessible interaction sites for the analyte compared with the U-shaped CPs (**2** and **3**). Thus, **4** exhibits the highest Stern–Volmer constant (K_{SV}) amongst all CPs. In Fig. S17 and S18, the plot and calculations for obtaining the K_{SV} values of **4** toward NFT and NFZ (6.77×10^4 M^{-1} and 5.86×10^4 M^{-1}, respectively) are shown. These high K_{SV} values are comparable with those of other pioneering MOFs reported in the literature.[20,22–50,63,64] In Tables S2 and S3, these values are listed.

The K_{SV} values of **1–3** toward NFT were compared with those of **4** (Fig. S19–S21). Notably, **1–3** exhibit lower K_{SV} values, amongst which **3** exhibits the highest quenching constant (3.74×10^4 M^{-1}), followed by **2** (3.48×10^4 M^{-1}) and **1** (3.22×10^4 M^{-1}). Hence, it can be concluded from the observations that for the efficient detection of NFT in aqueous media, a d^{10}-based MOCN, particularly a Cd(II)-based MOCN, is advantageous over a d^7- or d^8-based MOCN.

The 3D Stern–Volmer plot of **4** for all three classes of antibiotics is shown in Fig. S22. This plot highlights the selectivity of **4** toward NFT and NFZ amongst all other antibiotics at their low concentrations.

To determine the sensitivity of **4** in aqueous media toward NFT and NFZ, the limit of detection (LOD) was calculated using the following equation: LOD = $3\sigma/m$ (where σ is the standard deviation for five blank readings and m is the slope of the plots of intensity *vs.* concentration of the analyte). The LOD values of **4** toward NFT and NFZ are found to be as low as 197 (0.831 μmol L^{-1}) and 172 ppb (0.869 μmol L^{-1}), respectively (Fig. S23 and S24), with R^2 values of 0.975 and 0.9944, respectively. This indicates that **4** can efficiently detect a very trace amount of these analytes in aqueous media. These LOD values are comparable with those of other pioneering MOFs that were explored for the detection of NFT and NFZ in aqueous solutions (Tables S2 and S3).[20,22–50,63,64]

Furthermore, the sensitivity of **1–3** toward NFT was compared with that of **4**. Interestingly, they exhibit significantly larger LOD values than **4**, which follows the order: **1** (7.5 ppm or 31.7 μmol L^{-1}) ≫ **2** (695 ppb or 2.92 μmol L^{-1}) > **3** (373 ppb or

© 2026 The Author(s). Published by the Royal Society of Chemistry

Open Access Article. Published on 24 April 2026. Downloaded on 5/16/2026 2:45:13 AM.
This article is licensed under a Creative Commons Attribution-NonCommercial 3.0 Unported Licence.

1.57 μmol L^{-1}) > **4** (197 ppb or 0.831 μmol L^{-1}), as shown in Fig. S25–S27. Based on this comparative study, one can correlate the LOD values to the metal centers in **1–4**. Notably, the largest LOD value for **1** is due to the presence of paramagnetic Co(II) centers (its emission intensity is one order of magnitude less than that of the others). On the other hand, both Zn(II) and Cd(II) possess d^{10} electronic configurations, but the Cd(II)-based CP (**4**) adopts a V-shaped helical structure, which provides more accessible sites for interaction with the analyte compared with the Zn(II)-based CP (**3**), which exhibits U-shaped helicity. This difference in helicity plays an important role in host–guest interactions, which further affects their detection sensitivity. Thus, **4** exhibits a lower LOD value toward NFT than **3**. This observation signifies the role of a d^{10}-based MOCN in the detection of a very low concentration of nitrofuran-based antibiotics in water.

The competitive tests were carried out to assess the selective response of **4** toward NFT and NFZ in the presence of other interfering antibiotics. After titrating a suspension of **4** in water with 75 μL of any antibiotic solution other than NFT (Fig. 7a) and NFZ (Fig. 7b), the emission intensity drops to a minor extent. To this mixture, the addition of the same amount (75 μL) of NFT or NFZ results in a drastic drop in the emission intensity, which further supports our conclusion that **4** is sensitive and selective toward NFT or NFZ.

For any real-time application of a sensor, it is important that it exhibits ultrafast response times toward the target analyte. The emission intensity of **4** is quenched by 65% in the presence of 75 μL of NFT/NFZ within only 20 s. For the next 100 s, there is a subtle change in the emission intensity, proving the ultrafast detection of NFT or NFZ by **4** (Fig. 8 and Fig. S28).

Furthermore, test strips (made out of TLC plates) were soaked in an aqueous dispersion of **4** for 10–15 min and then air dried. Drop-casting 30 μL of 1 mM solutions of NFT or NFZ on the coated strips leads to the darkening of the spot under UV light, indicating the quenching of emission intensity of **4** by NFT/NFZ (Fig. 8, insets). The changes are visible to the naked eye, making this probe ideal for any real-time applications.

For the detection of both NFT and NFZ, **4** was recycled for up to five cycles. No significant change in the quenching percentage in both cases is noted up to the fifth cycle (Fig. S29 and S30). Furthermore, the similar PXRD patterns and FTIR spectra recorded before and after soaking **4** in an aqueous solution of NFT/NFZ for 24 h confirm that the coordination polymer remains unchanged during the fluorescence titration experiments (Fig. S31).

Next, we try to elaborate on the nature of the quenching process involved in the detection of such antibiotics by the sensors. In general, a quenching process can either be of a static or dynamic nature. For a static quenching process, a nonfluorescent sensor-analyte complex is formed at the ground state. As a result, due to the addition of different concentrations of the quencher, no significant change in the average lifetime of the species is observed. On the other hand, in dynamic quenching, the excited fluorophore collides with the quencher and gives away its excess energy in the form of a radiationless decay. This results in a change in the lifetime of the species

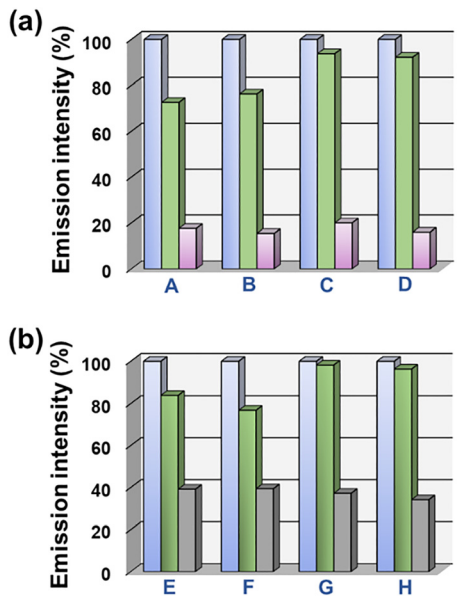

Fig. 7 Bar plots of the decrease in the emission intensity percentage of **4** before and after the addition of aqueous solutions of different antibiotics (75 μL), followed by the same amount of NFT (a) and NFZ (b). (Blue bars represent pristine **4**, green bars represent **4** + analyte, pink/grey bars represent **4** + analyte + NFT/NFZ; A: FDZ; E: ODZ; B/F: DMZ; C/G: SMZ; and D/H: SDZ.)

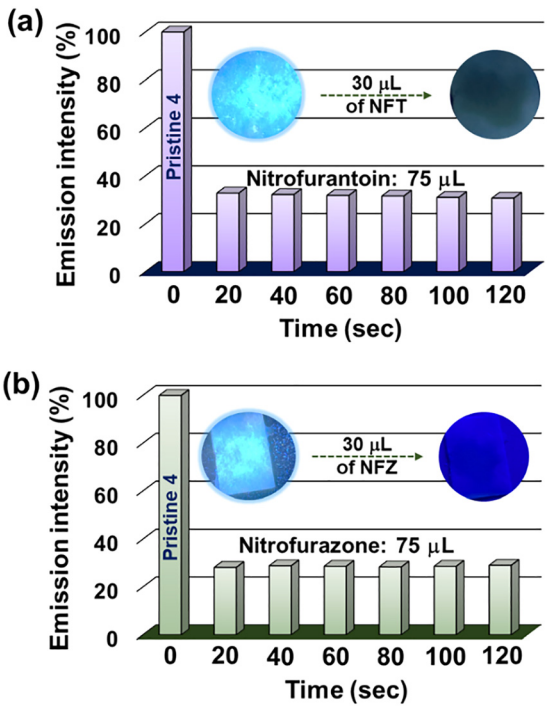

Fig. 8 (a) and (b) Ultrafast detection of NFT and NFZ by **4** in 20 s, respectively. Insets: Digital images of test paper strips encrusted with **4** before and after the addition of 30 μL of 1 mM solutions of NFT and NFZ prepared in Milli-Q water.

Open Access Article. Published on 24 April 2026. Downloaded on 5/16/2026 2:45:13 AM. This article is licensed under a Creative Commons Attribution-NonCommercial 3.0 Unported Licence.

with the concentration of the quencher. In order to determine the nature of quenching by NFT and NFZ, the time-resolved fluorescence studies were performed to calculate the average lifetime values of **4** before and after the addition of different concentrations of NFT and NFZ, respectively (Fig. S32 and Table S4). The average lifetime values of **4** in the presence of different concentrations of NFT and NFZ are as follows: for NFT: 0.121 ns (before NFT addition), 0.121 ns (after 50 μL NFT addition), 0.113 ns (after 100 μL NFT addition), and 0.09 ns (after 150 μL NFT addition); for NFZ: 0.121 ns (before NFZ addition), 0.107 ns (after 50 μL NFZ addition), 0.108 ns (after 100 μL NFZ addition), and 0.102 ns (after 150 μL NFZ addition). These values clearly indicate the involvement of both static and dynamic processes in the quenching phenomenon. This can confirm the formation of a nonfluorescent species between **4** and NFT/NFZ through a strong hydrogen bond between the nitrofurans and the oxadiazole moiety of **4**, as well as the collisions of excited **4** with the nitrofurans, resulting in a radiationless decay. The plots of average lifetime *vs.* volume of NFT/NFZ added are shown in Fig. S33.

Finally, the mechanism of action of **4** to selectively detect NFT and NFZ was considered. As mentioned earlier, supramolecular interactions like H-bonding and π···π interactions bring the sensor and the quenchers close to each other. In order to confirm the presence of such supramolecular interactions, similar fluorescence titration experiments in the presence of a 1 mM solution of NFT were carried out with $\{[Cd(mbhna)(bpma)]DMF\}_n$ (**5**) and $\{[Cd(3,7\text{-DBTDC})(bpma)]\cdot H_2O\}_n$ (**6**), which are the 3,7-DBTDC^{2-} and mbhna^{2-} congeners of **4**, respectively.[17,56] The flexible dicarboxylate, mbhna^{2-}, in **5** does not provide an option for H-bond acceptance from NFT, which is reflected in the lower quenching percentage (55%) and K_{SV} ($1.28 \times 10^4\ M^{-1}$) values and a LOD value of 547 ppb or 2.3 μmol L^{-1} (Fig. S34). On the other hand, **6**, constructed with the polar sulfone group bearing a rigid dicarboxylate, 3,7-DBTDC^{2-}, can interact with the –NH group of NFT through H-bond acceptance. Thus, $\{[Cd(3,7\text{-DBTDC})(bpma)]\ H_2O\}_n$ exhibits higher quenching (around 80%) in the presence of a 1 mM solution of NFT and exhibits a K_{SV} value of $3.4 \times 10^4\ M^{-1}$ and a LOD value of 317 ppb or 1.33 μmol L^{-1} (Fig. S35). These contrasting values corroborate well with our assumption that the H-bond between the sensor and the quencher plays an important role in the quenching process. The interaction of the sensor with the analytes through H-bonding is shown in Fig. S36.

Such supramolecular interactions also facilitate two processes, which play an important role in the quenching mechanism. These two processes are (a) fluorescence resonance energy transfer (FRET), in which energy is transferred between the sensor and the antibiotic, and (b) photo-induced electron transfer (PET), in which an electron travels from the electron-rich sensor to the electron-deficient analytes. The spectral overlap between the absorbance spectra of different classes of antibiotics and the emission spectrum of **4** was analyzed (Fig. 9a). An effective spectral overlap is observed for NFT, NFZ, and FDZ, whereas almost no overlap is observed for other antibiotics.[20] Furthermore, the absorption spectra of SMZ and SDZ are far apart from the emission spectrum of **4**, resulting in the lowest quenching. Fig. 9a clearly indicates the reason why the emission intensity of **4** is quenched to the maximum extent in the presence of the nitrofurans and to the lowest extent in the presence of the sulfonamides.

An electron, after excitation, travels from the conduction band (LUMO) of the fluorophore to the low-lying LUMO of the analyte instead of going back to its own ground state. This process is referred to as photo-induced electron transfer (PET). Quenching is observed when this electron from the low-lying LUMO of the analyte travels back to the ground state, losing the extra energy in the form of an emission. The involvement of PET in the quenching mechanism was assessed by density functional theory (DFT) calculations for the free ligand (H_2oxdz) and the antibiotics using the hybrid functional, Becke's three-parameter exchange, and the Lee–Yang–Parr correlation function (B3LYP) in the 6-31G(d,p) basis set of the Gaussian 09 program (Fig. 9b and Table S5).[65] The LUMOs of

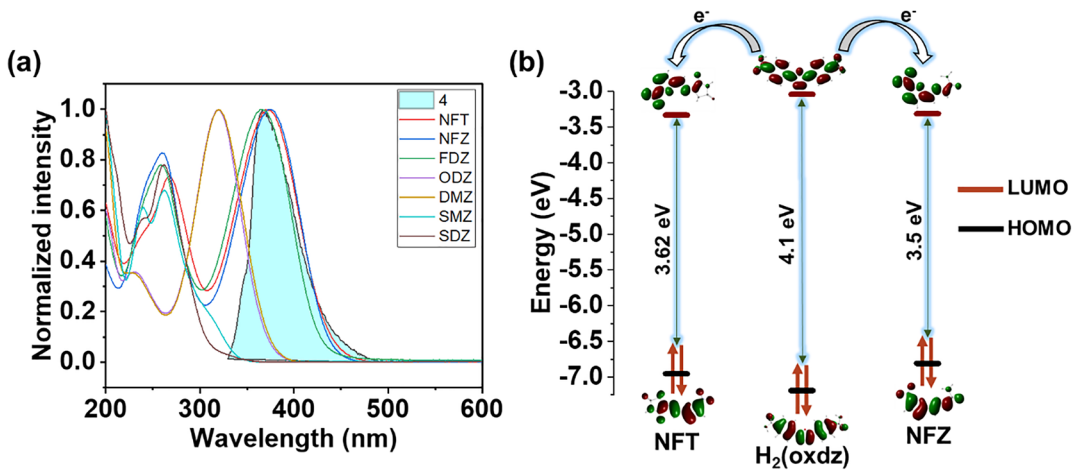

Fig. 9 (a) Spectral overlap between the emission spectrum of **4** and the absorption spectra of different antibiotics. (b) HOMO–LUMO energy levels of H_2(oxdz), NFT, and NFZ determined by DFT calculations using B3LYP in the 6-31G(d,p) basis set of the Gaussian 09 program.

© 2026 The Author(s). Published by the Royal Society of Chemistry

Open Access Article. Published on 24 April 2026. Downloaded on 5/16/2026 2:45:13 AM. This article is licensed under a Creative Commons Attribution-NonCommercial 3.0 Unported Licence.

NFT (−3.33 eV) and NFZ (−3.31 eV), as obtained from the DFT calculations, lie between the valence band (−7.19 eV) and conduction band (−3.04 eV) of H_2(oxdz). This arrangement of HOMO–LUMO energy levels facilitates easy migration of excited electrons from the conduction band to the LUMOs of NFT and NFZ, which results in quenching (Fig. 9b).[20] Such electron migration results in the redistribution of the HOMO–LUMO energy levels. The gap between the HOMO and LUMO energy levels of NFT/NFZ@H_2(oxdz) is found to be much less (3.14 and 3.12 eV, respectively) than that of H_2oxdz (4.15 eV), NFT (3.623 eV) and NFZ (3.5 eV). This is another indication of electron donation from H_2oxdz to NFT/NFZ (Fig. S37). Furthermore, it is observed that the lower the LUMO of the analyte, the greater the tendency of the electron to transit from the sensor to the analyte (Fig. S38 and Table S3). Amongst all the antibiotics, NFT and NFZ possess the lowest-lying LUMOs, and thus, easy electron transfer occurs from the conduction band of the sensor to the LUMO of NFT or NFZ, leading to the maximum quenching. On the other hand, since the LUMOs of SMZ and SDZ lie at higher energy levels compared with the conduction band of the sensor, no such electron transfer is possible. Thus, combining all these observations, it can be concluded that **4** exhibits the maximum quenching in the presence of NFT/NFZ, whereas it experiences the lowest quenching in the presence of the sulfonamides.

Conclusions

In summary, four luminescent 1D CPs, **1–4**, were synthesized following a one-pot self-assembly pathway utilizing an ancillary ligand (bpma), a dicarboxylate ($oxdz^{2-}$), and respective metal salts (Co(II), Ni(II), Zn(II), and Cd(II)) under ambient conditions. On the basis of their single-crystal structures, **2–4** display either U- or W-shaped 1D coordination polymer structures due to the different binding modes of the capping ligand (facial and meridional), the preferred coordination number of the metal ions, and the angularity and alignment of the bent oxadiazole dicarboxylate. Their thermal and chemical stabilities in different solvents and pH ranges were assessed by thermogravimetric analysis and powder X-ray diffraction. The luminescent properties of **1–4** were explored for the detection of nitrofuran-based antibiotics in aqueous media. After identifying the maximum turn-off quenching for **4**, it was further explored to obtain the quenching constant values for NFT and NFZ (6.77×10^4 M^{-1} and 5.86×10^4 M^{-1}, respectively). The low LOD values showed its ability to detect these antibiotics at the trace level in an aqueous medium. An in-depth analysis to explain the detection mechanism was performed with the help of time-resolved data, emission-absorption overlap observations, and theoretical evaluation. The selective and sensitive nature, recyclability, and ultrafast detection performance of **4** showcase its potential for the efficient detection of antibiotics and any other pharmaceutical products. Thus, further studies can be conducted under practical conditions in the future to investigate its applicability in mitigating other environmental issues.

Conflicts of interest

There are no conflicts to declare.

Data availability

The data supporting this paper are presented in this manuscript and the supplementary information (SI) file. The SI includes the materials and characterization methods, structural analyses and crystallographic tables for **2–4**, fluorescence titration plots, and K_{SV} and LOD comparison tables. See DOI: https://doi.org/10.1039/d6ma00033a.

CCDC 2520962 (**2**), 2520963 (**3**) and 2520964 (**4**) contain the supplementary crystallographic data for this paper.[66a–c]

Acknowledgements

This work was carried out with the financial assistance from IISER Mohali. For the senior research fellowship, A. C. is grateful to Ministry of Education, India. The authors acknowledge the use of the central facilities (X-ray, SEM and TEM) and other departmental facilities at IISER Mohali.

References

1 A. J. Browne, M. G. Chipeta, G. Haines-Woodhouse, E. P. A. Kumaran, B. H. K. Hamadani, S. Zaraa, N. J. Henry, A. Deshpande, R. C. Reiner, N. P. J. Day, A. D. Lopez, S. Dunachie, C. E. Moore, A. Stergachis, S. I. Hay and C. Dolecek, *Lancet Planet. Health*, 2021, **5**, e893–e904.

2 E. Y. Klein, T. P. Van Boeckel, E. M. Martinez, S. Pant, S. Gandra, S. A. Levin, H. Goossens and R. Laxminarayan, *Proc. Natl. Acad. Sci. U. S. A.*, 2018, **115**, E3463–E3470.

3 T. Defoirdt, P. Sorgeloos and P. Bossier, *Curr. Opin. Microbiol.*, 2011, **14**, 251–258.

4 Y. Song, J. Phipps, C. Zhu and S. Ma, *Angew. Chem., Int. Ed.*, 2023, **62**, e202216724.

5 Z. Zhang, H. Zhang, D. Tian, A. Phan, M. Seididamyeh, M. Alanazi, Z. P. Xu, Y. Sultanbawa and R. Zhang, *Coord. Chem. Rev.*, 2024, **498**, 215455.

6 F. Bessone, A. Ferrari, N. Hernandez, M. Mendizabal, E. Ridruejo, A. Zerega, F. Tanno, M. V. Reggiardo, J. Vorobioff, H. Tanno, M. Arrese, V. Nunes, M. Tagle, I. M. Caliz, M. R. Diaz, H. Niu, I. A. Alvarez, C. Stephens, M. I. Lucena and R. J. Andrade, *Arch. Toxicol.*, 2023, **97**, 593–602.

7 A. Leitner, P. Zöllner and W. Lindner, *J. Chromatogr. A*, 2001, **939**, 49–58.

8 S. P. Khong, E. Gremaud, J. Richoz, T. Delatour, P. A. Guy, R. H. Stadler and P. Mottier, *J. Agric. Food Chem.*, 2004, **52**, 5309–5315.

9 C. Blasco, A. D. Corcia and Y. Picó, *Food Chem.*, 2009, **116**, 1005–1012.

Open Access Article. Published on 24 April 2026. Downloaded on 5/16/2026 2:45:13 AM. This article is licensed under a Creative Commons Attribution-NonCommercial 3.0 Unported Licence.

10 D. Moreno-González, F. J. Lara, N. Jurgovská, L. Gámiz-Gracia and A. M. García-Campaña, *Anal. Chim. Acta*, 2015, **891**, 321–328.
11 M. Tabrizchi and V. ILbeigi, *J. Hazard. Mater.*, 2010, **176**, 692–696.
12 P.-L. Wang, L.-H. Xie, E. A. Joseph, J.-R. Li, X.-O. Su and H.-C. Zhou, *Chem. Rev.*, 2019, **119**, 10638.
13 S. Khan, P. Das and S. K. Mandal, *Inorg. Chem.*, 2020, **59**, 4588–4600.
14 P. Das and S. K. Mandal, *J. Mater. Chem. A*, 2018, **6**, 16246–16256.
15 N. Xu, Q. Zhang, B. Hou, Q. Cheng and G. Zhang, *Inorg. Chem.*, 2018, **57**, 13330–13340.
16 G. Chakraborty, P. Das and S. K. Mandal, *ACS Appl. Mater. Interfaces*, 2018, **10**, 42406–42416.
17 A. Chanda, S. Khullar and S. K. Mandal, *Eur. J. Inorg. Chem.*, 2021, 2595–2605.
18 Z. Zhang, Z. Wu, Z. Li, Y. Zhao, M. Yu, F. Jiang, L. Chen and M. Hong, *Cryst. Growth Des.*, 2023, **23**, 4491–4498.
19 A. Gogia and S. K. Mandal, *ACS Appl. Mater. Interfaces*, 2022, **14**, 16357–16368.
20 A. Chanda and S. K. Mandal, *Chem. – Asian J.*, 2025, **20**, e202401206.
21 A. Chanda and S. K. Mandal, *Dyes Pigm.*, 2023, **210**, 111025.
22 S. Mondal, R. Sahoo and M. C. Das, *Small*, 2025, **21**, 2409095.
23 P. R. Lakshni, P. Nanjan, S. Kannan and S. Shanmugaraju, *Coord. Chem. Rev.*, 2021, **435**, 213793.
24 S. Ghosh, A. Rana and S. Biswas, *Chem. Mater.*, 2024, **36**, 99–131.
25 B. Wang, X.-L. Lv, D. Feng, L.-H. Xie, J. Zhang, M. Li, Y. Xie, J.-R. Li and H.-C. Zhou, *J. Am. Chem. Soc.*, 2016, **138**, 6204–6216.
26 F. Zhang, H. Yao, T. Chu, G. Zhang, Y. Wang and Y. Yang, *Chem. – Eur. J.*, 2017, **23**, 10293–10300.
27 N. Xu, Q. Zhang, B. Hou, Q. Cheng and G. Zhang, *Inorg. Chem.*, 2018, **57**, 13330–13340.
28 Z. Zhang, Z. Wu, Z. Li, Y. Zhao, M. Yu, F. Jiang, L. Chen and M. Hong, *Cryst. Growth Des.*, 2023, **23**, 4491–4498.
29 X.-G. Liu, C.-L. Tao, H.-Q. Yu, B. Chen, Z. Liu, G.-P. Zhu, Z. Zhao, L. Shen and B. Z. Tang, *J. Mater. Chem. C*, 2018, **6**, 2983–2988.
30 M. Lei, F. Ge, X. Gao, Z. Shi and H. Zheng, *Inorg. Chem.*, 2021, **60**, 10513–10521.
31 R. Goswami, S. C. Mandal, N. Seal, B. Pathak and S. Neogi, *J. Mater. Chem. A*, 2019, **7**, 19471–19484.
32 Y.-M. Ying, C.-L. Tao, M. Yu, Y. Xiong, C.-R. Guo, X.-G. Liu and Z. Zhao, *J. Mater. Chem. C*, 2019, **7**, 8383–8388.
33 H. Li, J. Ren, X. Xu, L. Ning, R. Tong, Y. Song, S. Liao, W. Gu and X. Liu, *Analyst*, 2019, **144**, 4513–4519.
34 M. Lu, X. Xiao, S. Yu, W. Lin and Y. Yang, *Z. Anorg. Allg. Chem.*, 2022, **648**, e202100353.
35 F. Guo, C. Su, Y. Fan and W. Shi, *Dalton Trans.*, 2019, **48**, 12910–12917.
36 Y.-Q. Zhang, X.-H. Wu, S. Mao, W.-Q. Tao and Z. Li, *Talanta*, 2019, **204**, 344–352.
37 H.-W. Yang, P. Xu, B. Ding, Z.-Y. Liu, X.-J. Zhao and E.-C. Yang, *Eur. J. Inorg. Chem.*, 2019, 5077–5084.
38 Y. Zhou, Q. Yang, D. Zhang, N. Gan, Q. Li and J. Cuan, *Sens. Actuators, B*, 2018, **262**, 137–143.
39 Y. Su, Y. Guo, Q. Wu, L. Wang, Y. Wang, G. Yang, W. Zhang and Y. Wang, *Inorg. Chem.*, 2024, **63**, 15134–15143.
40 X. Li, S. Zhang, L. Zhang, Y. Yang, K. Zhang, Y. Cai, Y. Xu, Y. Gai and K. Xiong, *Cryst. Growth Des.*, 2022, **22**, 3991–3997.
41 Z.-L. Mu, Y.-Q. Ma, Y. Zhu, Z. Chen, H.-P. Xiao, X. Li, H.-Y. Wang and J.-Y. Ge, *Inorg. Chem.*, 2023, **62**, 20314–20324.
42 Q.-Q. Zhu, Q.-S. Zhou, H.-W. Zhang, W.-W. Zhang, D.-Q. Lu, M.-T. Guo, Y. Yuan, F. Sun and H. He, *Inorg. Chem.*, 2020, **59**, 1323–1331.
43 Q.-Q. Zhu, H. He, Y. Yan, J. Yuan, D.-Q. Lu, D.-Y. Zhang, F. Sun and G. Zhu, *Inorg. Chem.*, 2019, **58**, 7746–7753.
44 R. Goswami, S. C. Mandal, B. Pathak and S. Neogi, *ACS Appl. Mater. Interfaces*, 2019, **11**, 9042–9053.
45 P. Li, M.-Y. Guo, L.-L. Gao, X.-M. Yin, S.-L. Yang, R. Bu and E.-Q. Gao, *Dalton Trans.*, 2020, **49**, 7488–7495.
46 B. Li, Y.-Y. Jiang, Y.-Y. Sun, Y.-J. Wang, M.-L. Han, Y.-P. Wu, L.-F. Ma and D.-S. Li, *Dalton Trans.*, 2020, **49**, 14854–14862.
47 M. Fan, B. Sun, X. Li, Q. Pan, J. Sun, P. Ma and Z. Su, *Inorg. Chem.*, 2021, **60**, 9148–9156.
48 M. Yu, Y. Xie, X. Wang, Y. Li and G. Li, *ACS Appl. Mater. Interfaces*, 2019, **11**, 21201–21210.
49 F. Zhang, H. Yao, Y. Zhao, X. Li, G. Zhang and Y. Yang, *Talanta*, 2017, **174**, 660–666.
50 H. He, Q.-Q. Zhu, M.-T. Guo, Q.-S. Zhou, J. Chen, C.-P. Li and M. Du, *Cryst. Growth Des.*, 2019, **19**, 5228–5236.
51 Y. Tao, Q. Wang, Y. Shang, C. Yang, L. Ao, J. Qin, D. Ma and Z. Shuai, *Chem. Commun.*, 2008, 77–79.
52 Z. Li, W. Li, C. Keum, E. Archer, B. Zhao, A. M. Z. Slawin, W. Huang, M. C. Gather, I. D. W. Samuel and E. Zysman-Colman, *J. Phys. Chem. C*, 2019, **123**, 24772–24785.
53 M. Y. Wong, S. Krotkus, G. Copley, W. Li, C. Murawski, D. Hall, G. J. Hedley, M. Jaricot, D. B. Cordes, A. M. Z. Slawin, Y. Olivier, D. Beljonne, L. Muccioli, M. Moral, J.-C. Sancho-Garcia, M. C. Gather, I. D. W. Samuel and E. Zysman-Colman, *ACS Appl. Mater. Interfaces*, 2018, **10**, 33360–33372.
54 S. Khullar and S. K. Mandal, *Dalton Trans.*, 2015, **44**, 1203–1210.
55 A. Gogia, P. Das and S. K. Mandal, *ACS Appl. Mater. Interfaces*, 2020, **12**, 46107–46118.
56 A. Chanda and S. K. Mandal, *ACS Appl. Nano Mater.*, 2025, **8**, 12784–12798.
57 K. Nakamoto, *Infrared and Raman Spectra of Inorganic and Coordination Compounds*, John Wiley & Sons, New York, 5th edn, 1997.
58 H. Bhambri and S. K. Mandal, *ChemCatChem*, 2024, **16**, e202400429.
59 H. Bhambri and S. K. Mandal, *Inorg. Chem.*, 2024, **63**, 8685–8697.
60 A. W. Addison, T. Rao, J. Reedijk, J. V. Rijn and G. C. Verschoor, *Dalton Trans.*, 1984, 1349–1356.
61 A. Chanda and S. K. Mandal, *Inorg. Chem.*, 2024, **63**, 5598–5610.

© 2026 The Author(s). Published by the Royal Society of Chemistry

Open Access Article. Published on 24 April 2026. Downloaded on 5/16/2026 2:45:13 AM.
This article is licensed under a Creative Commons Attribution-NonCommercial 3.0 Unported Licence.

62 A. Gogia, H. Bhambri and S. K. Mandal, *J. Mater. Chem. A*, 2024, **12**, 6476–6487.
63 P. P. Mondal, D. Muthukumar, S. K. P. Fathima, R. S. Pillai and S. Neogi, *Cryst. Growth Des.*, 2023, **23**, 8342.
64 X. Yu, D. I. Pavlov, A. A. Ryadun, K. A. Kovalenko, A. S. Potapov and V. P. Fedin, *Inorg. Chem.*, 2025, **64**, 6356–6364.
65 M. J. Frisch, G. W. Trucks, H. B. Schlegel, G. E. Scuseria, M. A. Robb, J. R. Cheeseman, G. Scalmani, V. Barone, B. Mennucci, G. A. Petersson, H. Nakatsuji, M. Caricato, X. Li, H. P. Hratchian, A. F. Izmaylov, J. Bloino, G. Zheng, J. L. Sonnenberg, M. Hada, M. Ehara, K. Toyota, R. Fukuda, J. Hasegawa, M. Ishida, T. Nakajima, Y. Honda, O. Kitao, H. Nakai, T. Vreven, J. A. Montgomery Jr., J. E. Peralta, F. Ogliaro, M. Bearpark, J. J. Heyd, E. Brothers, K. N. Kudin, V. N. Staroverov, T. Keith, R. Kobayashi, J. Normand, K. Raghavachari, A. Rendell, J. C. Burant, S. S. Iyengar, J. Tomasi, M. Cossi, N. Rega, J. M. Millam, M. Klene, J. E. Knox, J. B. Cross, V. Bakken, C. Adamo, J. Jaramillo, R. Gomperts, R. E. Stratmann, O. Yazyev, A. J. Austin, R. Cammi, C. Pomelli, J. W. Ochterski, R. L. Martin, K. Morokuma, V. G. Zakrzewski, G. A. Voth, P. Salvador, J. J. Dannenberg, S. Dapprich, A. D. Daniels, O. Farkas, J. B. Foresman, J. V. Ortiz, J. Cioslowski and D. J. Fox, *Gaussian 09*, Gaussian, Inc., Wallingford, CT, 2013.
66 (*a*) CCDC 2520962: Experimental Crystal Structure Determination, 2026, DOI: 10.5517/ccdc.csd.cc2qm8c0; (*b*) CCDC 2520963: Experimental Crystal Structure Determination, 2026, DOI: 10.5517/ccdc.csd.cc2qm8d1; (*c*) CCDC 2520964: Experimental Crystal Structure Determination, 2026, DOI: 10.5517/ccdc.csd.cc2qm8f2.